Smectic Liquid-Crystalline Structure of Skyrmions in Chiral Magnet Co_{8.5}Zn_{7.5}Mn_{4}(110) Thin Film

T. Nagase, M. Komatsu, Y. G. So, T. Ishida, H. Yoshida, Y. Kawaguchi, Y. Tanaka, K. Saitoh, N. Ikarashi, M. Kuwahara, and M. Nagao

Smectic Liquid-Crystalline Structure of Skyrmions in Chiral Magnet Co$_{8.5}$Zn$_{7.5}$Mn$_4$(110) Thin Film

T. Nagase,[1*] M. Komatsu,[2] Y. G. So,[2] T. Ishida,[3] H. Yoshida,[4] Y. Kawaguchi,[5] Y. Tanaka,[5] K. Saitoh,[3] N. Ikarashi,[6,7] M. Kuwahara,[3*] and M. Nagao[6,7*]

[1]*Department of Electrical, Electronic Engineering and Information Engineering, School of Engineering, Nagoya University, Nagoya 464-8601, Japan*

[2]*Department of Materials Science, Graduate School of Engineering Science, Akita University, Akita 010-8502, Japan*

[3]*Advanced Measurement Technology Center, Institute of Materials and Systems for Sustainability, Nagoya University, Nagoya 464-8601, Japan*

[4]*Department of Physics, Hokkaido University, Sapporo 060-0810, Japan*

[5]*Department of Applied Physics, Graduate School of Engineering, Nagoya University, Nagoya 464-8601, Japan*

[6]*Center for Integrated Research of Future Electronics, Institute of Materials and Systems for Sustainability, Nagoya University, Nagoya 464-8601, Japan*

[7]*Department of Electronics, Graduate School of Engineering, Nagoya University, Nagoya 464-8603, Japan*

*Correspondence to: nagase.tomoki@k.mbox.nagoya-u.ac.jp, kuwahara@imass.nagoya-u.ac.jp, nagao.masahiro@imass.nagoya-u.ac.jp

Abstract

Organizing of magnetic skyrmions shows several forms similar to atomic arrays of solid states. Using Lorentz transmission electron microscopy, we report the first direct observation of a stable liquid-crystalline structure of skyrmions in chiral magnet $Co_{8.5}Zn_{7.5}Mn_4(110)$ thin film, caused by magnetic anisotropy and chiral surface twist. Elongated skyrmions are oriented and periodically arranged only in the <110> directions, whereas they exhibit short-range order along the <001> directions, indicating smectic skyrmion state. In addition, skyrmions possess anisotropic interaction with opposite sign depending on the crystal orientation, in contrast to existing isotropic interaction.

Topological objects, such as vortices, skyrmions, merons, and monopoles, are typically shown to order or disorder states [1-11], analogous to atomic arrays of solid states because of their particlelike properties. For example, triangular and square vortex lattices have been observed in type-II superconductors [1,2]. Another representative example is magnetic skyrmions, which have been attracted interest because of their emergent electromagnetism and spintronics applications [12,13]. Skyrmions condense into close-packed two-dimensional triangular lattice [3-5].

Magnetic anisotropy plays a key role in skyrmion arrays of chiral magnets. In B20-type chiral magnets [3-5] with very weak magnetic anisotropies, the triangular skyrmion crystal (tri-SkX) is always formed by application of the magnetic field irrespective of the crystal orientation. On the other hand, recent studies for bulk chiral magnets have demonstrated skyrmion states as square lattice in β-Mn-type $Co_8Zn_8Mn_4$ [6] and amorphous form in multiferroic Cu_2OSeO_3 [7]. Such states are caused by a relatively large magnetic anisotropy.

Another fascinating aspect of skyrmion properties is nanostructural characteristics induced by noncollinear spin modulations near the edge/surface of chiral magnets, the so-called chiral edge/surface twist [14-18]. This can be understood as micromagnetic Neumann boundary conditions (NBCs) of the ferromagnetic and Dzyaloshinskii-Moriya interactions [14]. In the nanowires and nanodisks, the chiral edge twist leads to peculiar skyrmion morphology and formation [19-21].

As described above, skyrmions typically show some forms similar to atomic arrays of solid states, such as the triangular lattice, square lattice, and amorphous states. Although other different skyrmion states as the hexatic state under skyrmion-lattice melting transition [4] and moving liquid-crystalline skyrmion state under electric currents [22-24] have been suggested, the realization of soft-matter skyrmions including dynamic and static states remains unchallenged due to a lack of theoretical and experimental investigations. In this Letter, we report the first observation of a stable static two-dimensional smectic liquid-crystalline structure of skyrmions using Lorentz transmission

electron microscopy (LTEM). This is caused by the magnetic anisotropy and the chiral surface twist in a β-Mn-type $Co_{8.5}Zn_{7.5}Mn_4$(110) thin film. In addition, the continuous change to skyrmion chains occurs by further application of the magnetic field to the smectic skyrmion state. These behaviors indicate the coexistence of attractive and repulsive interactions between skyrmions depending on the crystal orientations.

We prepared the $Co_{8.5}Zn_{7.5}Mn_4$(110) thin film with the thickness of $t \sim 100$ nm. The cubic Co-Zn-Mn has the magnetic easy axes of the <100> directions [6,25-27]. In the $Co_{8.5}Zn_{7.5}Mn_4$(110) thin film, one easy axis is parallel to the in-plane direction and the other two are at an angle of 45-degree to the in-plane direction. Besides, the Co-Zn-Mn shows a relatively long helical period (L_D) [26]. The depth of the chiral surface twist is proportional to L_D [16]. Figure 1(a) shows simulated magnetization angle from the wavefront (θ) in the helical spin order with $L_D = 70$ nm (FeGe) [5] and $L_D = 145$ nm ($Co_{8.5}Zn_{7.5}Mn_4$) in a thin film of $t = 100$ nm (see also Supplemental Material [28]). As seen in Fig. 1(a), the chiral surface twist is supposed to be dominant and expected to affect the skyrmion state in the $Co_{8.5}Zn_{7.5}Mn_4$ thin film with $t \sim 100$ nm.

The bulk sample was prepared by a conventional melting process. The thin film for the LTEM observations was prepared by Ar-ion milling method. The thickness of the thin film was estimated by electron energy-loss spectroscopy. Observations of magnetic structures were performed using the Fresnel mode of LTEM (JEOL JEM2100F) with the specimen-heating double-tilting holder. We obtained the LTEM images after taking enough time to stabilize the temperature. In addition, the displayed specimen temperature has been calibrated. All the fast Fourier transform (FFT) patterns were obtained from LTEM images with the region of 6×6 μm^2.

Figure 1(b) is a low-magnification LTEM image at the magnetic field of $B = 160$ mT applied normal to the film at 334 K. The image was obtained in the wedge-shaped thin film where the thickness varies from ~150 nm (left) to ~100 nm (right). Figure 1(b) clearly demonstrates the

thickness-dependence of the skyrmion state. The boundary of the skyrmion states exists around the center of the image. In the thick region, skyrmions assemble into the cluster state with the conventional tri-SkX, whereas in the thin region, they are sparse as shown in the enlarged images of Figs. 1(c) and 1(d). The thickness-dependence is collateral evidence that the sparse skyrmion state results from the effect of the chiral surface twist. Note that the sparse skyrmion state is formed without passing through the conventional skyrmion state and shows a different distribution of skyrmions every time we do experiments in the same region. To compare the skyrmion states in the thick ($t \sim 200$ nm) and thin ($t \sim 100$ nm) regions, we display the phase diagrams in Figs. 1(e) and 1(f), respectively. The no magnetic contrast at zero magnetic field in spite of less than magnetic transition temperature (T_C) appears in the thick and thin regions. The previous LTEM study on Co-Zn-Mn thin film has already reported similar behavior [26]. In the thick region ($t \sim 200$ nm), skyrmions form conventional tri-SkX (see also Supplemental Material [28]). The existence region of the tri-SkX cluster state in $t \sim 150$ nm [the left side in Fig. 1(b)] is essentially the same as that of the tri-SkX in $t \sim 200$ nm. It is noteworthy that, the phase diagram of the thin region [Fig. 1(f)] shows two unconventional skyrmion states: amorphous and sparse (smectic) skyrmions. We focus on the skyrmion phases in the thin region that follows.

Figure 2 shows a series of the LTEM images at 344 K near T_C in the thin region ($t \sim 100$ nm). As shown in Fig. 2(a), the stripe contrasts with a period of 145 nm are visible at zero magnetic field. With increasing B, the fuzzy dot-like contrasts appear in the stripe contrasts [the arrows in Fig. 2(b)], which are identified as skyrmions or unformed ones. By further increasing B, skyrmions are formed, however, no tri-SkX is formed [Fig. 2(c)]. The FFT pattern [the inset of Fig. 2(c)] is discerned in the halo feature, indicating the amorphous skyrmion state. This is caused by the different sizes and shapes of each skyrmion. There is a divergence in the existing mechanism of which the skyrmion size is determined by the strength ratio of the ferromagnetic exchange interaction to the

5

Dzyaloshinskii-Moriya interaction. In bulk chiral magnets, the cause of the amorphous skyrmions has been discussed in the effect of the magnetic anisotropy [7] or the magnetic frustration [8]. In the present case, the amorphous skyrmions appear at high temperatures (341 K - 344 K), indicating that the magnetic frustration cannot seem to be involved in the formation. In addition, skyrmions form triangular lattice in the thick region ($t \sim 200$ nm). Therefore, it is possible that the observed amorphous skyrmions may be caused by a combination of the magnetic anisotropy and the chiral surface twist. At 115 mT, the magnetic contrasts disappear [Fig. 2(d)] because of the transition to the ferromagnetic state.

We observed another unconventional skyrmion state. Figure 3 shows a series of the LTEM images at 334 K. At zero magnetic field, Fig. 3(a) shows the stripe contrasts. As shown in Fig. 3(b), the stripe contrasts disappear at 130 mT. At 140 mT, skyrmions begin to appear from the no magnetic contrast regions [Fig. 3(c)], and then they proliferate in the whole region at 160 mT [Fig. 3(d)]. Although the number of skyrmions reaches a maximum value at 160 mT, the skyrmion density is low, corresponding to Fig. 1(b). Some blurred contrasts are due to local movement of skyrmions through thermal fluctuation. Apparently, the sparse skyrmion state is neither amorphous nor lattice states on a closer look.

We characterize the sparse skyrmion state by examining their configurations and shape. Figure 4(a) shows the FFT pattern obtained from the LTEM image of the sparse skyrmions at 160 mT. The spatial-frequency spectra along <110> directions are sharp, on the other hand, those along <110> directions are broad. They mean that the sparse skyrmion state has long-range order along the <110> directions, whereas, short-range order along the <001> directions. Moreover, we obtained a highly-resolved LTEM image, by controlling the defocus value (Δf), as shown in Fig. 4(b). The image clearly shows that skyrmions are elongated and oriented only in the <110> directions. Note that we confirmed that the elongated magnetic contrasts arise from the magnetization textures of

skyrmions [28]. These crystal-orientation-dependences are obviously induced by the magnetic anisotropy. It is important that our experimental results [Figs. 4(a) and (b)] are reminiscent of the *smectic-A liquid-crystal* [29,30].

Although the sparse skyrmion state appears identical to the smectic skyrmion state, we could not rule out another possibility. Specifically, the sparse skyrmion state has a basic structure of the primitive or face-centered rectangle lattices with the stacking faults along the <110> directions. Given this, there are the hidden peaks within the streaks along <110> directions in the FFT pattern. To determine whether the sparse skyrmion state has the hidden basic structure or smectic structure, we analyzed the LTEM images for the distances (d_{sk}) [Fig. 4(c)] and angular orientation (θ_{sk}) [Fig. 4(d)] of adjacent skyrmions using Delaunay triangulation statistics [31]. The area is uniquely divided into triangles on condition that no skyrmion is inside the circumcircle of any triangle. Distributions of d_{sk} and θ_{sk} are determined by counting all the lengths of the sides and the angles of triangles, respectively. If the sparse skyrmion state has a basic structure, most of the divided triangles should agree with the following parameters; d_{sk} = 210 nm, 278 nm, 348 nm, and θ_{sk} = 37°, 53°, 90° for the primitive rectangle lattice (red arrows in Figs. 4(c) and 4(d)), or d_{sk} = 210 nm, 297 nm, 297 nm, and θ_{sk} = 42°, 69°, 69° for the face-centered rectangle lattice (green arrows), presumed by the FFT pattern [28]. If the sparse skyrmion state has a basic structure, the values indicated by the arrows in Figs. 4(c) and 4(d) should become a local maximum. However, our analysis results clarify that there are no characteristic peaks. Thus, we conclude that the sparse skyrmion state has no basic structure and has the smectic liquid-crystalline structure. Recently, electronic liquid-crystalline phases have attracted attention in the field of condensed matter physics [32-35]. Moreover, although the presence of static stable liquid-crystalline superconducting vortices has intensively been investigated [36-41], no conclusive evidence has been provided. Our finding is therefore the first direct observation of the stable liquid-crystalline structure of topological objects.

Incidentally, the amorphous skyrmion state is continuously connected with the smectic skyrmion state. The halo FFT pattern [the inset in Fig. 2(c)] is non-uniform. The intensity of spatial-frequency spectra around the <110> and <001> directions are higher, that is similar to Fig. 4(a). In fact, the amorphous skyrmions continuously change to the smectic skyrmions with increasing B at 342 K [28].

By further increasing B from the smectic skyrmion state at 160 mT, skyrmions gradually decline and continuously change to skyrmion chains along the <110> directions [Figs. 5(a) and 5(b)]. At 220 mT, the skyrmion chains disappear [Fig. 5(c)]. Figure 5(d) shows the B-dependence of the q-values along <110> and <001> directions obtained from FFT patterns. The q-values along <110> directions are almost unchanged, whereas q-values along <110> directions continue to decrease with increasing field. In the real-space, the smectic skyrmion state changes to isolate skyrmion chains with increasing magnetic field while keeping long-range order along the <110> directions. In addition, it is suggested that the skyrmion chains are a thermal-equilibrium state because they reappear with decreasing the magnetic field from 220 mT [28].

We consider the interaction of skyrmions in the smectic skyrmions and the skyrmion chains. Recent studies on B20-type FeGe have revealed the sign change of the interactions depending on the magnetic field: attractive force at low fields and repulsive force at high fields [42]. On the other hand, our results indicate the sign change depending on the crystal orientation. In the thin region ($t \sim 100$ nm), the skyrmion chains along the <110> directions strongly retain the long-range order without the change of the skyrmion distance, ranging from low to high magnetic fields. While skyrmions along the <001> directions retain the short-range order without the aggregation of the skyrmion chains. These behaviors indicate that there is a persistence of attractive interaction along the <110> directions even at high magnetic fields and repulsive interaction along <001> directions. These anisotropic skyrmion interactions are different from existing skyrmion interactions. Although many

theoretical works have investigated current and thermal response of skyrmions to understand and predict skyrmion dynamics [22-24,43,44], they have been based on a particle model with isotropic skyrmion interactions on the bases of the existing experimental results. The anisotropic skyrmion interactions that we revealed have the potential to generate unconventional dynamics and provide a new avenue for next-generation spintronics devices [45-49]. On the other hand, in the thick region ($t \sim 200$ nm) and the bulk Co-Zn-Mn, thermal-equilibrium skyrmion state is conventional tri-SkX [6,8,26,27,50] i.e., the skyrmion interaction is isotropic. Furthermore, it has been reported that the tri-SkX in the magnetic thin film of FeGe ($t \sim 30$ nm) [5] and Fe/Gd multilayers [51] with weak magnetic anisotropy, where the surface twist is dominant. Therefore, the observed behaviors are induced by the combination of the magnetic anisotropy and the chiral surface twist.

Finally, we propose the theoretical model to further understand our results. We performed the micromagnetic simulation considering the fourth-order cubic magnetocrystalline anisotropy [28]. However, our simulation results in the tri-SkX distorted along <001> directions with a circular shape. We think that the anisotropic exchange interaction [52,53] has to be also considered. As described above, the chiral surface twist can be modeled by the micromagnetic NBCs [14,28]. If the exchange interaction is anisotropic, an anisotropic magnetic twist state caused by anisotropic NBCs [28] is expected at near the surface of chiral magnets. Although the anisotropic exchange interaction is usually weak, it possibly affects magnetic structures in a thin film of chiral magnets where the chiral surface twist is dominant. Unfortunately, at the present moment, the parameters of both the cubic magnetocrystalline anisotropy and the anisotropic exchange interaction are unknown. Further experimental and theoretical works are therefore necessary to understand our results. In addition, thermodynamic theoretical model [3,7] is also necessary to understand temperature-dependent skyrmion states, that is, amorphous and smectic skyrmion states.

In summary, we have demonstrated the smectic liquid-crystalline structure of skyrmions. This

is the first direct observation of a stable liquid-crystalline structure of topological objects. The LTEM observations revealed the coexistence of attractive and repulsive skyrmion interactions. These skyrmions have anisotropic interactions and have the potential to generate unconventional current- and thermal-driven skyrmion dynamics beyond existing skyrmions with isotropic interactions. Furthermore, this study provides a new avenue for controlling the properties of topological objects.

References

[1] A. Tonomura, H. Kasai, O. Kamimura, T. Matsuda, K. Harada, Y. Nakayama, J. Shimoyama, K. Kishio, T. Hanaguri, K. Kitazawa, M. Sasase, and S. Okayasu, Nature (London) **412**, 620-622 (2001).

[2] R. Gilardi, J. Mesot, A. Drew, U. Divakar, S. L. Lee, E. M. Forgan, O. Zaharko, K. Conder, V. K. Aswal, C. D. Dewhurst, R. Cubitt, N. Momono, and M. Oda, Phys. Rev. Lett. **88**, 217003 (2002).

[3] S. Mühlbauer, B. Binz, F. Jonietz, C. Pfleiderer, A. Rosch, A. Neubauer, R. Georgii, and P. Böni, Science **323**, 915-919 (2009).

[4] X. Z. Yu, Y. Onose, N. Kanazawa, J. H. Park, J. H. Han, Y. Matsui, N. Nagaosa, and Y. Tokura, Nature (London) **465**, 901-904 (2010).

[5] X. Z. Yu, N. Kanazawa, Y. Onose, K. Kimoto, W. Z. Zhang, S. Ishiwata, Y. Matsui, and Y. Tokura, Nat. Mater. **10**, 106–109 (2011).

[6] K. Karube, J. S. White, N. Reynolds, J. L. Gavilano, H. Oike, A. Kikkawa, F. Kagawa, Y. Tokunaga, H. M. Rønnow, Y. Tokura, and Y. Taguchi, Nat. Mater. **15**, 1237-1242 (2016).

[7] A. Chacon, L. Heinen, M. Halder, A. Bauer, W. Simeth, S. Mühlbauer, H. Berger, M. Garst, A.

Rosch, and C. Pfleiderer, Nat. Phys. **14**, 936-941 (2018).

[8] K. Karube, J. S. White, D. Morikawa, C. D. Dewhurst, R. Cubitt, A. Kikkawa, X. Z. Yu, Y. Tokunaga, T. Arima, H. M. Rønnow, Y. Tokura, and Y. Taguchi, Sci. Adv. **4**, eaar7043 (2018).

[9] X. Z. Yu, W. Koshibae, Y. Tokunaga, K. Shibata, Y. Taguchi, N. Nagaosa, Y. Tokura, and Nature (London) **564**, 95-98 (2018).

[10] T. Tanigaki, K. Shibata, N. Kanazawa, X. Z. Yu, Y. Onose, H. S. Park, D. Shindo, and Y. Tokura, Nano Lett. **15** 5438-5442 (2015).

[11] Y. Fujishiro, N. Kanazawa, T. Nakajima, X. Z. Yu, K. Ohishi, Y. Kawamura, K. Kakurai, T. Arima, H. Mitamura, A. Miyake, K. Akiba, M. Tokunaga, A. Matsuo, K. Kindo, T. Koretsune, R. Arita, and Y. Tokura, Nat.Commun. **10**, 1059 (2019).

[12] N. Nagaosa and Y. Tokura, Nat. Nanotechnol. **8**, 899–911 (2013).

[13] A. Fert, N. Reyren, and V. Cros, Nat. Rev. Mater. **2**, 17031 (2017).

[14] S. Rohart and A. Thiaville, Phys. Rev. B **88**, 184422 (2013).

[15] M. N. Wilson, E. A. Karhu, D. P. Lake, A. S. Quigley, S. Meynell, A. N. Bogdanov, H. Fritzsche, U. K. Roßler, and T. L. Monchesky, Phys. Rev. B **88**, 214420 (2013).

[16] S. A. Meynell, M. N. Wilson, H. Fritzsche, A. N. Bogdanov, and T. L. Monchesky, Phys. Rev. B **90**, 014406 (2014).

[17] S. L. Zhang, G. van der Laan, W.W. Wang, A. A. Haghighirad, and T. Hesjedal, Phys. Rev. Lett. **120**, 227202 (2018).

[18] D. Song, Z. A. Li, J. Caron, A. Kovács, H. Tian, C. Jin, H. Du, M. Tian, J. Li, J, Zhu, and R. E. Dunin-Borkowski, Phys. Rev. Lett. **120**, 167204 (2018).

[19] H. Du, R. Che, L. Kong, X. Zhao, C. Jin, C. Wang, J. Yang, W. Ning, R. Li, C. Jin, X. Chen, J. Zang, Y. Zhang, and M. Tian, Nat. Commun. **6**, 8504 (2015).

[20] C. Jin, Z. A. Li, A. Kovács, J. Caron, F. Zheng, F. N. Rybakov, N. S. Kiselev, H. Du, S. Blügel,

M. Tian, Y. Zhang, M. Farle, and R. E Dunin-Borkowski, Nat. Commun. **8**, 15569 (2017).

[21] F. Zheng, H. Li, S. Wang, D. Song, C. Jin, W. Wei, A. Kovács, J. Zang, M. Tian, Y. Zhang, H. Du, and R. E. Dunin-Borkowski, Phys. Rev. Lett. **119**, 197205 (2017).

[22] C. Reichhardt and C. J. Olson Reichhardt, Phys. Rev. B **94**, 094413 (2016).

[23] C. Reichhardt and C. J. Olson Reichhardt, Rep. Prog. Phys. **80**, 026501 (2017).

[24] S. A. Díaz, C. J. O. Reichhardt, D. P. Arovas, A. Saxena, and C. Reichhardt, Phys. Rev. B **96**, 085106 (2017).

[25] W. Xie, S. Thimmaiah, J. Lamsal, J. Liu, T. W. Heitmann, D. Quirinale, A. I. Goldman, and V. Pecharsky, G. J. Miller, J. Inorg. Chem. **52**, 9399-9408 (2013).

[26] Y. Tokunaga, X. Z. Yu, J. S. White, H. M. Rønnow, D. Morikawa, Y. Taguchi, and Y. Tokura, Nat. Commun. **6**, 7638 (2015).

[27] D. Morikawa, X. Z. Yu, K. Karube, Y. Tokunaga, Y. Taguchi, T.-h. Arima, and Y. Tokura, Nano Lett. **17**, 1637-1641 (2017).

[28] See Supplemental Material for LTEM images, micromagnetic simulation, magnetization textures of the smectic skyrmions, details of the Delaunay triangulation statistics, and the micromagnetic Neumann boundary conditions, which includes Refs. [54-57].

[29] L. V. Azároff, Mol. Cryst. Liq. Cryst. **60**, 73-98 (1980).

[30] K. Okoshi, T. Hagihara, M. Fujiki, and J. Watanabe, Liq. Cryst. **37**, 1183-1190 (2010).

[31] A. Soumyanarayanan, M. Raju, A. L. Gonzalez Oyarce, A. K. C. Tan, M. Y. Im, A. P. Petrovic, P. Ho1, K. H. Khoo, M. Tran1, C. K. Gan, F. Ernult, and C. Panagopoulos, Nat. Mater. **16**, 898-904 (2017).

[32] H. Tsunetsugu and M. Arikawa, J. Phys. Soc. Jpn. **75**, 083701 (2006).

[33] R. A. Borzi, S. A. Grigera, J. Farrell, R. S. Perry, S. J. S. Lister, S. L. Lee, D. A. Tennant, Y. Maeno, and A. P. Mackenzie, Science **315,** 214 (2007).

[34] S. Kasahara, H. J. Shi, K. Hashimoto, S. Tonegawa, Y. Mizukami, T. Shibauchi, K. Sugimoto, T. Fukuda, T. Terashima, Andriy H. Nevidomskyy, and Y. Matsuda, Nature (London) **486**, 382-385 (2012).

[35] S. Yonezawa, K. Tajiri, S. Nakata, Y. Nagai, Z. Wang, K. Segawa, Y. Ando, and Y. Maeno, Nat. Phys. **13**, 1074-1078 (2017).

[36] G. Blatter, B. I. Ivlev, and J. Rhyner, Phys. Rev. Lett. **66**, 2392 (1991).

[37] L. Balents and D. R. Nelson, Phys. Rev. Lett. **73**, 2618 (1994).

[38] L. Balents and D. R. Nelson, Phys. Rev. B **52**, 12951 (1995).

[39] A.A. Zhukov, H. Kupfer, G. K. Perkins, A.D. Caplin, T. Wolf, K.I. Kugel, A.L. Rakhmanov, M.G. Mikheev, V. I. Voronkova, M. Klaser, and H. Wuhl, Phys. Rev. B **59**, 11213 (1999).

[40] S. Gordeev, A. Zhukov, P. de Groot, A. Jansen, R. Gagnon, and L. Taillefer, Phys. Rev. Lett. **85**, 4594 (2000).

[41] I. Guillamón, H. Suderow, A. F. Pacheco, J. Sese, R. Cordoba, J. M. Teresa, M. R. Ibarra, and S. Vieira, Nat. Phys. **5**, 651 (2009).

[42] H. Du, X. Zhao, F. N. Rybakov, A. B. Borisov, S. Wang, J. Tang, C. Jin, C. Wang, W. Wei, N. S. Kiselev, Y. Zhang, R. Che, S. Blügel, and M. Tian, Phys. Rev. Lett. **120**, 197203 (2018).

[43] S.-Z. Lin, C. Reichhardt, C. D. Batista, and A. Saxena, Phys. Rev. B **87**, 214419 (2013).

[44] C. Reichhardt, D. Ray, and C. J. Olson Reichhardt, Phys. Rev. Lett. **114**, 217202 (2015).

[45] D. Pinna, G. Bouriano, and K. Everschor-Sitte, arXiv:1811.12623.

[46] G. Bourianoff, D. Pinna, M. Sitte, and K. Everschor-Sitte, AIP Adv. **8**, 055602 (2018).

[47] D. Prychynenko, M. Sitte, Ks. Litzius, B. Krüger, G. Bourianoff, M. Kläui, J. Sinova, and K. Everschor-Sitte, Phys. Rev. Appl. **9**, 014034 (2018).

[48] D. Pinna, F. Abreu Araujo, J.-V. Kim, V. Cros, D. Querlioz, P. Bessiere, J. Droulez, and J. Grollier, Phys. Rev. Appl. **9**, 064018 (2018).

[49] J. Zázvorka, F. Jakobs, D. Heinze, N. Keil, S. Kromin, S. Jaiswal, K. Litzius, G. Jakob, P. Virnau, D. Pinna, K. Everschor-Sitte, L. Rózsa, A. Donges, U. Nowak, and M. Kläui, Nat. Nanotech. **14**, 658–661 (2019).

[50] K. Karube, J. S. White, D. Morikawa, M. Bartkowiak, A. Kikkawa, Y. Tokunaga, T. Arima, H. M. Rønnow, Y. Tokura, and Y. Taguchi, Phys. Rev. Mater. **1**, 074405 (2017).

[51] S. A. Montoya, R. Tolley, I. Gilbert, S. G. Je, M. Y. Im, and E. E. Fullerton, Phys. Rev. B **98**, 104432 (2018).

[52] S. D. Yi, S. Onoda, N. Nagaosa, and J. H. Han, Phys. Rev. B **80**, 054416 (2009).

[53] F. Qian, L. J. Bannenberg, H. Wilhelm, G. Chaboussant, L. M. Debeer-Schmitt, M. P. Schmidt, A. Aqeel, T. T. M. Palstra, E. Brück1, A. J. E. Lefering, C. Pappas, M. Mostovoy, and A. O. Leonov, Sci. Adv. **4**, eaat7323 (2018).

[54] A. Vansteenkiste, J. Leliaert, M. Dvornik, M. Helsen, F. Garcia-Sanchez, and B. Van Waeyenberge, AIP Adv. **4**, 107133 (2014).

[55] M. Beg, R. Carey, W. Wang, D. Cort´es-Ortuño, M. Vousden, M.-A. Bisotti, M. Albert, D. Chernyshenko, O. Hovorka, R. L. Stamps, and H. Fangohr, Sci. Rep. **5**, 17137 (2015).

[56] K. Ishizuka and B. Allman, J. Electron Microsc. **54**, 191 (2005).

[57] K. Shibata, A. Kovács, N. S. Kiselev, N. Kanazawa, R. E. Dunin-Borkowski, and Y. Tokura, Phys. Rev. Lett. **118**, 087202 (2017).

Acknowledgments

Competing interests

The authors declare no competing interests.

Figure legends

FIG. 1. Thickness-dependent skyrmion states. (a) Simulated magnetization angle from the wavefront (θ) in the helical spin order in t = 100 nm for L_D = 70 nm (FeGe, blue dot) and L_D = 145 nm ($Co_{8.5}Zn_{7.5}Mn_4$, red dot). The z is normal to the surface. (b) Low-magnification under-focused LTEM image (Δf = 2 mm). The thickness varies from $t \sim$ 150 nm (left) to $t \sim$ 100 nm (right). (c) and (d) The enlarged views of the green (c) and red (d) dotted box areas in (b). (e) and (f) Phase diagrams of B versus T obtained in $t \sim$ 200 nm (e) and $t \sim$ 100 nm (f) regions. Sk stands for the skyrmion. The filled circles and squares indicate the measurement points. The filled squares in (f) are correspond to the LTEM images in Figs. 1(b), 1(d), 2, 3, 4(b), and 5.

FIG. 2. Formation of amorphous skyrmions. (a)-(d) Over-focused LTEM images (Δf = +2 mm) obtained in the thin region ($t \sim$ 100 nm) at 344 K and 0 mT (a), 50 mT (b), 85 mT (c), and 115 mT (d). The scale bars are 200 nm. Fuzzy dot-like contrasts in (b) are indicated by the arrows. The regions enclosed by the red lines in (c) correspond to a skyrmion. The inset in (c) shows the FFT pattern. The scale bar in the inset is 5 μm [1].

FIG. 3. Formation of sparse (smectic) skyrmions. (a)-(d) Under-focused LTEM images (Δf = 2 mm) obtained in the thin region ($t \sim 100$ nm) at 334 K and 0 mT (a), 130 mT (b), 140 mT (c), and 160 mT (d). The scale bars are 500 nm. Blurred contrasts in (d) are due to the local movement of skyrmions during the exposure of 5 sec.

FIG. 4. Analysis of sparse skyrmions. (a) The FFT pattern of the LTEM image of the sparse skyrmions. (b) Highly-resolved under-focused LTEM image of the sparse skyrmion (Δf = 750 μm) obtained in the thin region ($t \sim 100$ nm). (c) and (d) Real-space analysis of skyrmion configurations for the distances (d_{sk}) and angles (θ_{sk}) of adjacent skyrmions obtained from the Delaunay triangulation statistics. The total sample size is 1944. The red and green arrows point the values of the assumed primitive and face-centered rectangle lattice constants, respectively.

FIG. 5. Magnetic field dependence of the skyrmion chains. (a)-(c) Under-focused LTEM images (Δf = 2 mm) obtained in the thin region ($t \sim 100$ nm) at 334 K and at 200 mT (a), 210 mT (b), and 220 mT (c). The scale bars are 500 nm. (d) Magnetic field dependence of the $\boldsymbol{q}$-values along <110> directions (q_{110} blue dots) and <001> directions (q_{001} red dots) obtained from the FFT patterns. (e) and (f) The FFT patterns at 170 mT (e) and 195 mT (f).

(a) Angle θ (deg) vs z (nm); $L_D = 70$ nm (blue), $L_D = 145$ nm (red); upper surface, lower surface

(b) 334 K, 160 mT; [001], [$\bar{1}$10]; 1 µm

(e) Magnetic Field B (T) vs Temperature T (K): Ferromagnetic, Sk + Ferromagnetic, Stripe, Triangular SkX, No Contrast, Paramagnetic

(f) Magnetic Field B (T) vs Temperature T (K): Ferromagnetic, Stripe, Smectic Sk, Stripe + Sk, Condensed Amorphous Sk, Sk + Stripe, No Contrast, Stripe, Paramagnetic

Figure 1   LE17538   19AUG2019

(a) 0 mT, 200 nm

(b) 50 mT

(c) 85 mT

(d) 115 mT

[001]
[1̄10]
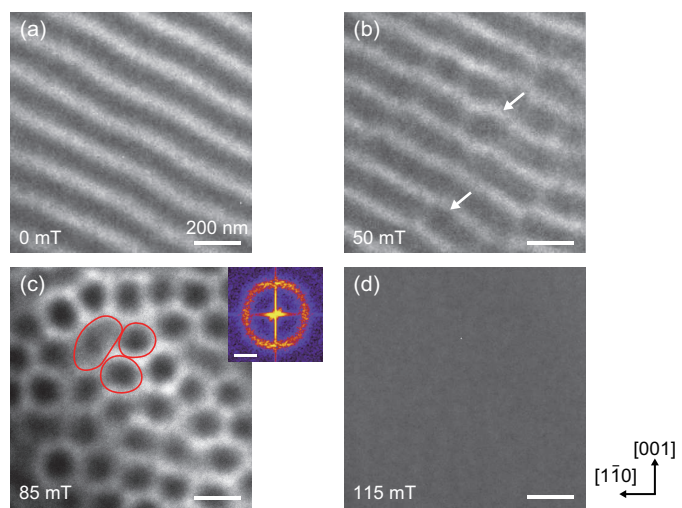
Figure 2   LE17538   19AUG2019

(a) 0 mT 500 nm

(b) 130 mT

(c) 140 mT

(d) 160 mT [001] [1̄10]
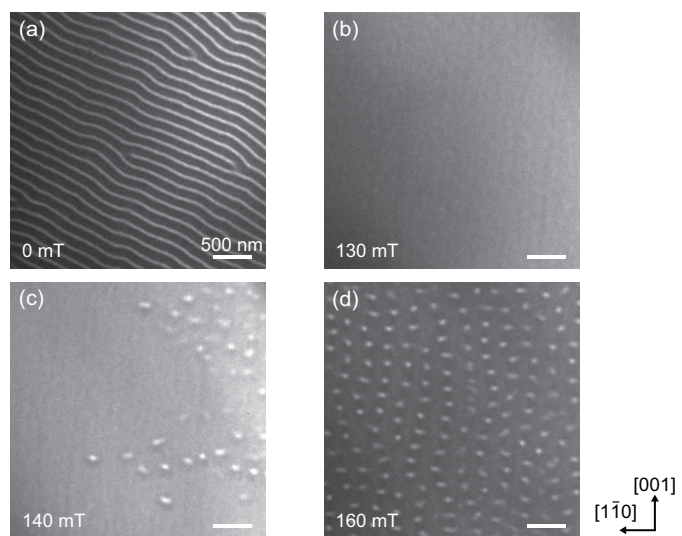
Figure 3   LE17538   19AUG2019

(a)

5 μm⁻¹

(b)   334 K
       160 mT

200 nm   [001]
                      [1̄10]

(c)

Frequency (%)

Distances d_{sk} (nm)

(d)

Frequency (%)

Angles θ_{sk} (deg)
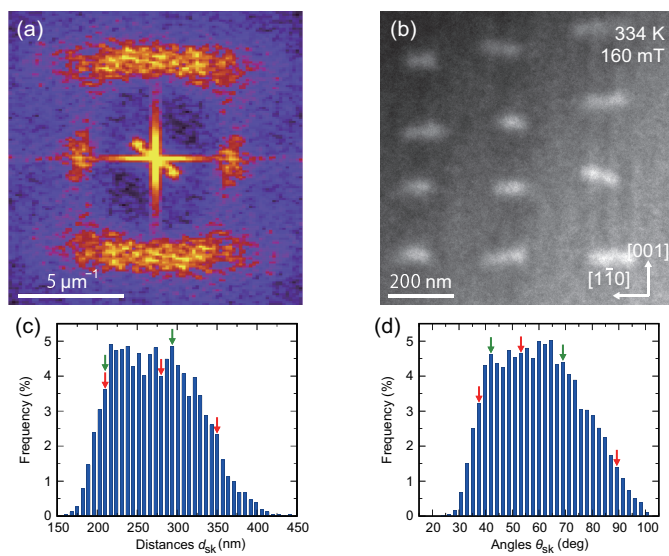
Figure 4   LE17538   19AUG2019

(a) 200 mT 500 nm
(b) 210 mT
(c) 220 mT

[001]
[1$\bar{1}$0]

(d)
q-values (μm^{-1})
q_{110}
q_{001}

Magnetic Field B (T)

(e) 170 mT 5 μm^{-1}
(f) 195 mT

Figure 5   LE17538   19AUG2019